PCCP
Physical Chemistry Chemical Physics

Accepted Manuscript

This article can be cited before page numbers have been issued, to do this please use: X. Lv, F. Li, J. Gong, J. Gu, S. Lin and Z. Chen, *Phys. Chem. Chem. Phys.*, 2020, DOI: 10.1039/D0CP00967A.

This is an Accepted Manuscript, which has been through the Royal Society of Chemistry peer review process and has been accepted for publication.

Accepted Manuscripts are published online shortly after acceptance, before technical editing, formatting and proof reading. Using this free service, authors can make their results available to the community, in citable form, before we publish the edited article. We will replace this Accepted Manuscript with the edited and formatted Advance Article as soon as it is available.

You can find more information about Accepted Manuscripts in the Information for Authors.

Please note that technical editing may introduce minor changes to the text and/or graphics, which may alter content. The journal's standard Terms & Conditions and the Ethical guidelines still apply. In no event shall the Royal Society of Chemistry be held responsible for any errors or omissions in this Accepted Manuscript or any consequences arising from the use of any information it contains.

ROYAL SOCIETY OF CHEMISTRY

rsc.li/pccp

View Article Online
DOI: 10.1039/D0CP00967A

Metallic FeSe Monolayer as Anode Materials for Li and Non-Li Ion Batteries: A DFT Study

Xiaodong Lv,[1] Fengyu Li,[1,*] Jian Gong,[1,*] Jinxing Gu,[2] Shiru Lin,[2]

Zhongfang Chen[2,*]

[1] *Physical School of Science and Technology, Inner Mongolia University, Hohhot, China, 010021*

[2] *Department of Chemistry, The Institute for Functional Nanomaterials, University of Puerto Rico, Rio Piedras Campus, San Juan, PR 00931, USA*

*corresponding author: fengyuli@imu.edu.cn (FL); ndgong@imu.edu.cn (JG); zhongfangchen@gmail.com (ZC)

DOI: 10.1039/D0CP00967A

Abstract

By means of density functional theory computations, we explored the electrochemical performance of the monolayer FeSe as anode materials for lithium and non-lithium ion batteries (LIBs and NLIBs). The electronic structure, adsorption, diffusion, and storage behavior of different metal atoms (*M*) in FeSe were systematically investigated. Our computations revealed that M adsorbed FeSe (M = Li, Na and K) systems show metallic characteristics which give rise to a good electrical conductivity, and mobility with low activation energy for diffusion (0.16, 0.13 and 0.11 eV for Li, Na, and K, respectively) in the transportation of electrons and metal atoms in materials, indicative of a fast charge/discharge rate. In addition, the theoretical capacities of the FeSe monolayer for Li, Na and K reach up to 658, 473, 315 mA h g^{-1}, respectively, higher than that of commercial graphite (372 mA h g^{-1} for Li, 284 mA h g^{-1} for Na, 273 mA h g^{-1} for K), and the average open-circuit voltage is moderate (0.38~0.88 V for Li, Na and K). All these characteristics suggest the FeSe monolayer is a potential anode material for alkali-metal rechargeable batteries.

Keywords: Lithium-ion batteries, Non-lithium ion batteries, Density functional theory, FeSe monolayer, Anode materials

View Article Online
DOI: 10.1039/D0CP00967A

1. Introduction

Among the numerous energy devices, rechargeable lithium-ion batteries (LIBs) are playing an indispensable role from portable electronic devices to electric vehicles,[1–4] and may offer excellent environment-friendly transportation and energy storages for renewable energy sources in the very near future. However, the source of lithium on earth is rather limited: based on the current consumption rate of 20280 tons per year, the lithium source can only be maintained for up to 65 years.[5] Consequently, Non-lithium ion batteries (NLIBs), such as sodium (Na), potassium (K), magnesium (Mg) and calcium (Ca) ion batteries (NIBs, KIBs, MIBs, and CIBs), are being actively explored[6–14] because of their higher abundances and the similar electrochemical mechanisms to LIBs. Nevertheless, the superior performances of metal ion batteries are limited by, among others, the lack of suitable anode materials with low-cost and high capacity, short charge-discharge time and long cycle life.[15]

In this regard, two-dimensional (2D) materials, having novel chemical and physical properties and high surface-to-volume ratio, are promising as excellent anode materials of LIBs and NLIBs.[16–18] Various 2D materials, such as graphene, transition metal oxides (TMOs) and chalcogenides (TMDs), phosphorene, and MXenes, have been investigated as anode materials.[19–26] Among these 2D materials, TMDs are fairly easy to prepare in large scale and naturally abundant, which make them attractive candidates for anode materials. It has been experimentally proved MoS_2, a TMD with unique sandwiched structure, has a good performance as LIBs with high specific capacity and low diffusion.[27,28] However, MoS_2 monolayer is a semiconducting with a considerable band gap of ~ 1.80 eV,[29] though it can be used as electrode especially when combined with more conducting materials,[30] the lack of good intrinsic conductivity would limit its electrochemical performances.

Recently, Liu *et al.* and co-workers successfully synthesized 47 high-quality monolayer transition-metal chalcogenides (TMDs) and heterostructures.[31] Among them, the binary compound FeSe monolayer is metallic with a spin-polarized ground state,[32] thus has an excellent electronic conductivity. Since the discovery of possible high-temperature superconductivity in monolayer FeSe,[33,34] tremendous efforts have been devoted to increasing its superconducting transition temperature (T_c).[35–41] The superconductive FeSe monolayer can also exhibit topological phase transition. Among others, Wang *et al*. demonstrated that the high-temperature 2D superconductor FeSe monolayer exhibits an antiferromagnetic (AFM) quantum spin Hall (QSH) state and QSH-to-quantum anomalous Hall (QAH) phase transition depending on the handedness of light.[42,43] Very recently, Lei *et al*.[44] developed a field-effect transistor (FET) device using a solid ion conductor (SIC) as the gate dielectric, which can tune the carrier density of FeSe by driving lithium ions in and out of the FeSe thin flakes and consequently control the physical properties and phase transitions.

Beyond the unique superconducting properties, the performance of layered FeSe as electrode materials for metal-ion batteries was also explored. Experimentally, Wei *et al.* demonstrated that the layer structure α-FeSe is very promising as anode material for rechargeable lithium batteries: a safe discharging voltage at ~ 1.5 V versus Li^+/Li and sustainable reversible capacity of 340 mA h g^{-1} after 40 cycles.[45] Koike's group found that layered FeSe has the potential to function as the anode in sodium-ion batteries, and they successfully synthesized Li-intercalated $Li_yFeSe_{1-x}Te_x$ using the electrochemical technique.[46,47] Kim *et al.* showed that the solid state Li-ion batteries with FeSe anode have the high-rate capability and cycle performance owing to the small particle size.[48] Theoretically, Jiang *et al.* examined the intercalation and

View Article Online
DOI: 10.1039/D0CP00967A

diffusion of alkali ions (Li^+, Na^+, K^+) in FeSe bulk, and found that the diffusion energy path of Li^+ in FeSe has a low activation barrier (0.20 eV), a flat discharging curve of Li^+ are obtained at 1.0 V. These results indicate XFe_2Se_2 (X = Li^+) may be potential electrochemical active material.[49]

Compared with the three-dimensional FeSe bulk materials, the 2D FeSe monolayer has even superior characteristics, such as the larger surface/volume ratio, improved electrochemical kinetics, and reversibility. Thus, it is highly possible that using FeSe monolayer as anode materials can greatly improve the performance of metal-ion batteries. In this work, by means of systematic density functional theory (DFT) computations, we carefully examined the adsorption and diffusion of various metal atoms (Li, Na, K, Mg, and Ca) on the FeSe monolayer, and investigated the storage capacity and open circuit voltage of the FeSe monolayer anode. Our computations showed that the FeSe monolayer is indeed a potential anode material for Li-, Na- and K-ion batteries.

2. Computational Methods

In this study, the spin-polarized DFT computations methods within the Vienna *ab initio* simulation package (VASP) was used.[50–52] The plane wave basis set with an energy cut-off of 600 eV and generalized gradient approximation (GGA) in the form of the Perdew-Burke-Ernzerhof (PBE) exchange correction functional was also employed. [53,54] A dispersion scheme, the Grimme-D2 method was used to describe the van der Waals (vdW) interactions,[55] A Monkhorst-Pack scheme [56] of 5×5×1 *k*-point of the 2×2×1 supercell was used in all the calculations. To illustrate the atomistic structures and charge densities, we used the VESTA package.[57]

The adsorption of Li, Na, K, Mg, and Ca adatoms were stimulated over FeSe supercell under periodic boundary conditions in all direction. An inter-layer vacuum

space larger than 20 Å was used to avoid interactions of mirror images in adjacent layers. The optimized structure was acquired by employing the convergence criteria were set at 1×10^{-6} eV per atom in energy and 0.02 eV $Å^{-1}$ in force. To more precisely calculate the final values, charge densities, electronic density of states (DOS) using the tetragonal methods with Blöchl corrections in which the Brillouin zone was sampled with a 15×15×1 Monkhorst *k*-point mesh size. To evaluate charge transfer between the ions and the FeSe sheet, we performed the Bader charge analysis.[58,59] In order to investigate the metal atoms diffusion behavior on the FeSe monolayer, the climbing-image nudged elastic band (CI-NEB) methods [60,61] was used to search the minimum energy pathway between the given initial and final configurations. The cell and the structures were fully relaxed during the calculation of the adsorption/diffusion process for Li/Na/K/Mg/Ca atoms.

Being aware of the strong correlation effects in iron compounds,[62] we also adopted the PBE+U method (U = 4 eV, J = 1 eV for Fe) [63] to investigate the magnetic/electronic properties of FeSe monolayer and the Li adsorption/diffusion behavior as well as the theoretical storage capacity of Li on the FeSe sheet. We found that both PBE and PBE+U give the antiferromagnetic and metallic character of the ground state of FeSe monolayer (Fig.1 and Fig. S1); Among the three examined adsorption sites (**A**, **B** and **C**), PBE+U and PBE predict the same trend of energetic preference of Li adsorption, and almost the same relative adsorption strength (Table S1). The calculated Li diffusion barrier of path **A-C-A** by PBE+U (0.96 eV) is also very close to that at PBE level (0.95 eV). Moreover, both methods yield the same theoretical specific capacity of 658 mAh g^{-1}. These test computations showed that the differences between the PBE+U and PBE methods for our examined systems are

View Article Online
DOI: 10.1039/D0CP00967A

insignificant. Thus, we used spin-polarized PBE method throughout the calculations in this work unless stated otherwise.

The thermal stability of FeSe monolayer (a 5×5×1 supercell) was evaluated by the first-principles molecular dynamics (FPMD) simulations in NVT ensemble lasting for 5 *ps* with a time step of 0.5 fs, the temperature was controlled by using the Nosé-Hoover method,[64] where the Nosé mass Q = 0.1 and M = 2 were adopted. The thermal expansion was not considered, and the Brillouin zone integration was applied using Gamma point during the FPMD simulations.

3. Results and Discussion

3.1. Structural and electronic properties, and stability of the FeSe monolayer

First, we examined the structure, stability and electronic properties of monolayer FeSe. From the top view, the monolayer FeSe sheet exhibits a typical tetragonal structure with the space group P4/nmm symmetry; from the side view, the FeSe sheet possesses a three-atomic-layer structure with one Fe sublayer sandwiched by two Se sublayers, and each Fe/Se atom is surrounded by four Se/Fe atoms.

Note that the energetically most favorable antiferromagnetic configuration was adopted for the FeSe monolayer in this study.[32] In its optimized structure (Fig. 1a), each unit cell consists of four Fe atoms and four Se atoms. The optimized structural parameters of monolayer FeSe are $a = b$ = 5.32 Å (Fig. S1), in good agreement with previous theoretical data (~ 5.34 Å).[32] The calculated Fe–Se bond lengths are uniformly 2.36 Å, and the Fe–Se–Fe and Se–Fe–Se bond angles are 68.60° and 111.40°, respectively.

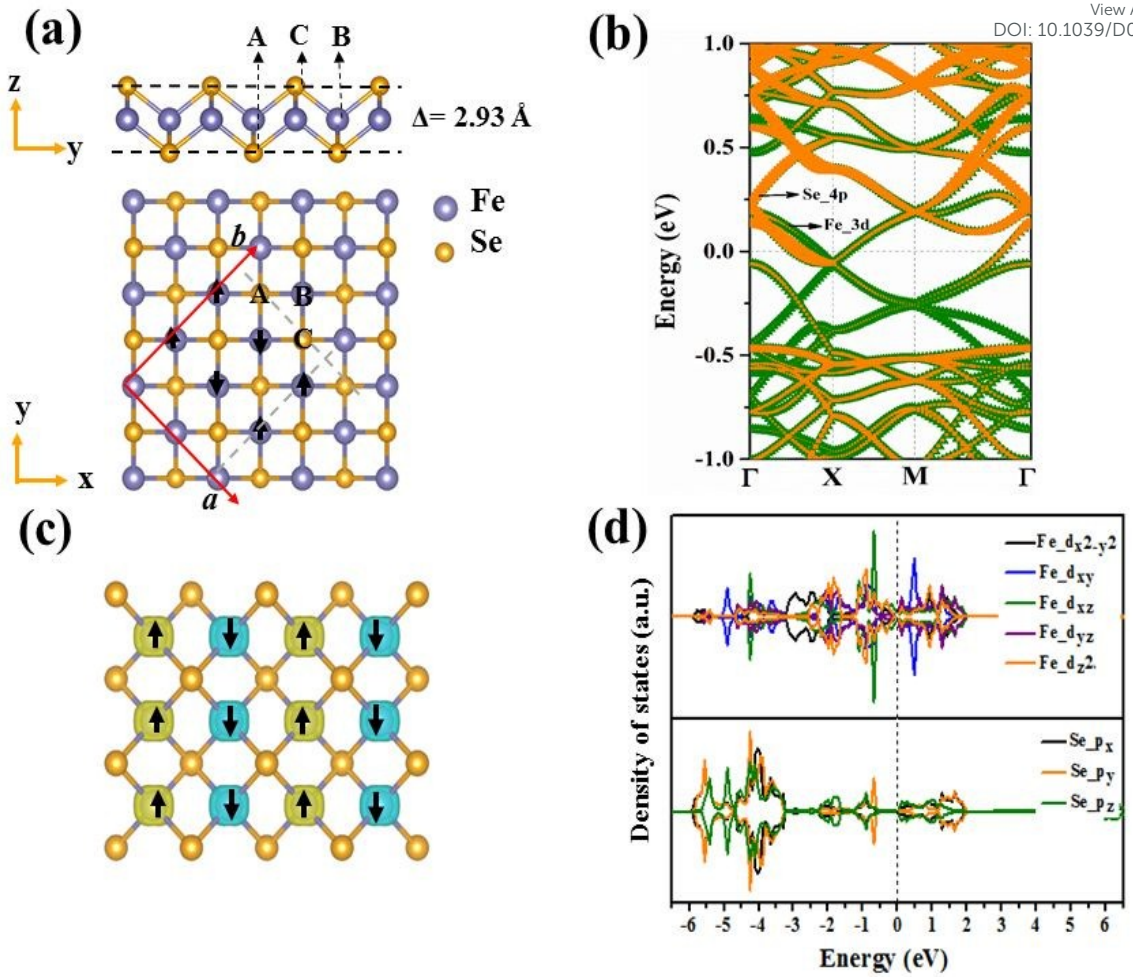

Fig. 1 (a) The optimized geometric structure (side and top views), (b) the band structure, (c) the spatial spin density distribution (top views), and (d) the projected density of states (PDOS) of FeSe monolayer. In Figure (b), the gold and green curves denote the *p* orbits of the Se atoms and the *d* orbits of Fe atoms, respectively, and the thickness of the curves represents the weight of atomic orbital contribution to the band structure. The Fermi level is denoted by a dashed line.

Though the monolayer FeSe grown on $SrTiO_3$ was confirmed to be thermodynamically and kinetically stable,[65] its thermal stability at high temperatures has not been studied yet. Thus, we assessed the thermal stability with a 5×5×1 supercell of monolayer FeSe at selected temperatures of 500 K, 700 K, 1000 K and 1500 K by performing first principles molecular dynamics (FPMD) simulations,

respectively (Fig. S2). The FeSe monolayer does not collapse throughout the 5 *ps* MD simulation up to 1000 K, and even does not disrupt up to 1500 K, there is no significant deformation or bond breakage. When the structure obtained through 5 ps FPMD simulation at 1500 K was re-optimised, the distorted FeSe monolayer quickly recover its original configuration, implying its good thermal stability and is feasible for practical applications.

We also considered the mechanical properties of the FeSe monolayer, the elastic constants and in-plane Young's modules (*Y*) were investigated (Table S2 and Fig. S4). The in-plane Young's modulus (79.03 N/m) is smaller than the *Y* value of the single-layer MoS_2 (124.39 N/m, computed at the same level of theory), indicating less energy variation in expansion during intercalation.

The electronic and magnetic property of electrode materials strongly correlates with the battery cyclability and rate performance. Therefore, we calculated the electronic band structures, spatial spin density distribution, and projected density of states (PDOS) of FeSe monolayer at the PBE level (Fig. 1). Note that most TMD monolayers, including MoS_2, are semiconducting with moderate band gaps, implying relatively low electrical conductivity as electrode materials. Our computations revealed that the FeSe monolayer is antiferromagnetic with single-stripe order (Fig. 1c) at the ground state, and each Fe atom carries the magnetic moment of 2.01 μ_B, agreeing well with previous predictions.[32] The FeSe monolayer shows metallic character as indicated by the electronic states crossing the Fermi level (Fig. 1b), and the states near the Fermi level originate mainly from the Fe 3*d* orbitals (Fig. 1d). The metallic character of the FeSe monolayer offers an intrinsic advantage in electrical conductivity and a satisfying electrochemical property for better battery cycling.

3.2. The adsorption of the single metal (*M*, *M* = Li, Na, K, Mg, and Ca) atom on the FeSe monolayer

To evaluate the diffusion and storage properties of the metal atoms (*M*) on the surface of FeSe monolayer, we investigated the preferred adsorption site of the *M* atom (*M* = Li, Na, K, Mg, and Ca). There are three possible high symmetry adsorption sites, namely the **A**, **B**, and **C** sites (Fig. 1a), for one M atom to be adsorbed on the FeSe sheet. At site **A** (**C**), the metal atom sits over the Se atom of the bottom (top) Se layer, and bonds with four (one) Se atoms, respectively. At site **B**, the metal atom locates over the Fe atom and bonds with two Se atoms. To determine the preferred adsorption site, we calculated the adsorption energy, where a large 2×2×1 supercell was used to avoid the interactions between the adjacent metal atoms. The adsorption energy (E_{ads}) of a metal atom on the monolayer is defined as:

$$E_{ads} = E_{M/FeSe} - E_{FeSe} - E_{M} \quad (1)$$

where the $E_{M/FeSe}$ and E_{FeSe} are the energies of the FeSe supercell with and without the adsorbed metal atom, respectively, and E_M represents the energy of an isolated M atom. According to this definition, a more negative adsorption energy indicates a more favorable exothermic reaction between FeSe and metal atoms.

Almost all the investigated metal atoms can be effectively adsorbed on the FeSe monolayer, as indicated by the negative E_{ads} values (Fig. 2, Table S3). For all metal atoms, the site **A** is the energetically most favored adsorption site, which is ascribed to the significantly larger number of M–Se bonds at the site **A** (four M–Se bonds). The corresponding E_{ads} values at **A** sites are −2.75, −2.29, −2.28, −1.65, and −2.26 eV for Li, Na, K, Mg, and Ca, respectively. These much negative adsorption energies guarantee the strong adsorption of metal atoms on the FeSe monolayer.

View Article Online
DOI: 10.1039/D0CP00967A

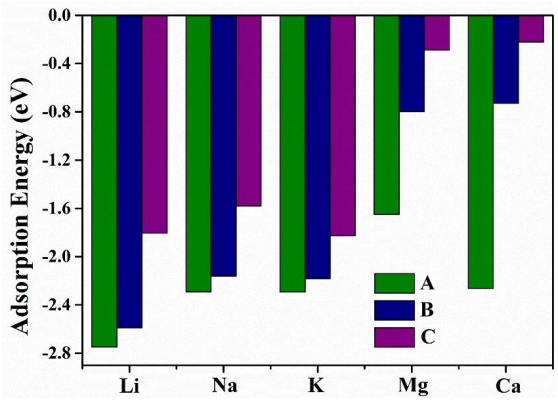

Fig. 2 The adsorption energies of single metal atoms (*M* = Li, Na, K, Mg, and Ca) on the FeSe monolayer at the three examined adsorption sites **A**, **B**, and **C**.

Fig. 3 presents the optimized structures for M-adsorbed FeSe monolayers (*M* = Li, Na, K, Mg, and Ca) at **A** sites. For the case of Li/Na/K adsorption, the Li/Na/K–Se bond length is 2.72/2.90/3.24 Å, the adsorption height (*h*), i.e., the vertical distance between Fe sublayer and Li/Na/K is 1.88/2.66/3.38 Å. For Mg- and Ca-adsorbed configurations, the Mg–Se and Ca–Se bond lengths are 2.70 and 2.87 Å, the adsorbed heights for Mg and Ca are 2.15 and 2.60 Å, respectively. The corresponding configurations at **B** and **C** sites were given in Fig. S5 and S6. Obviously, in the same group, M atom with larger atomic number has longer M–Se bond length and larger adsorption height (*h*) with the increase of atomic radii. The adsorption energy of Li, Na, and K are inversely proportional to the atomic radii, where Li has the highest E_{ads} value. Therefore, we can conclude that the general trend of the alkali adatoms (Li, Na, K) adsorption on monolayer FeSe can be predicted through their atomic radii: a smaller radius indicates a higher adsorption energy and thus a strong attachment of the adatom to the surface of the FeSe, and *vice versa*. However, Mg and Ca do not follow the same trend regarding to the atomic radii, probably due to their divalent metal ion nature.

View Article Online
DOI: 10.1039/D0CP00967A

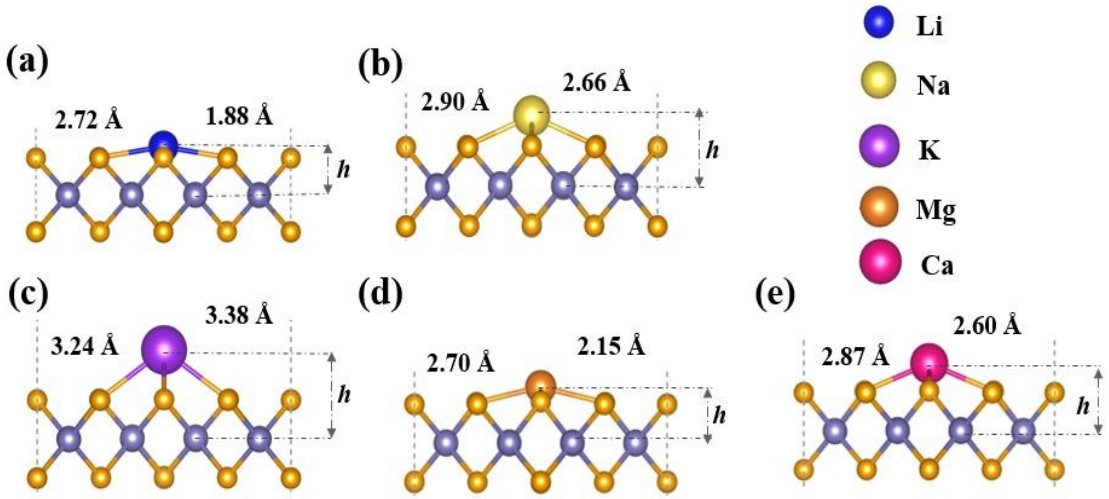

Fig. 3 Sides views of the optimized structures of FeSe monolayer after adsorption with (a) Li, (b) Na, (c) K, (d) Mg, and (e) Ca at **A** site.

A deep insight into the adsorption process can be obtained by investigating the charge density difference between bare and adsorbed FeSe monolayer using the following formula,

$$\Delta\rho = \rho_{M/FeSe} - \rho_{FeSe} - \rho_{M} \qquad (2)$$

where $\rho_{M/FeSe}$ and ρ_{FeSe} denote the total electron densities of the relaxed FeSe monolayer with and without metal atoms, respectively, and ρ_{M} is the total electron density of the metal atom. Fig. 4 and Fig. S7 present the charge density difference plots for M atoms at **A** sites (the plots for **B** and **C** sites were given in Fig. S8 and Fig. S9), in which the electron-accumulating region (yellow) is located between metal atoms and FeSe monolayer, while the electron-depleting region (blue) is around metal atoms, suggesting that all the adsorbed metal atoms behave as electron donors, i.e., the adsorbed metal atoms transfer electrons to the FeSe monolayer, which originates from the stronger electronegativity of Se than those metal atoms (Li, Na, K, Mg, and Ca). According to Bader charge analysis (Table S4), the electrons transferred from Li, Na,

View Article Online
DOI: 10.1039/D0CP00967A

K, Mg, and Ca to the FeSe monolayer at **A** sites are 0.93, 0.91. 0.92, 1.52, and 1.39 e^-, respectively, which are quite close to the charge transfer of these metal atoms to Cl in their chlorides (0.92, 0.86, 0.88, 1.61 and 1.56 e^- for LiCl, NaCl, KCl, $MgCl_2$ ad $CaCl_2$, respectively), suggesting the charge state of "+1 (+2)" for the adsorbed Li, Na and K (Mg and Ca) on the FeSe monolayer.

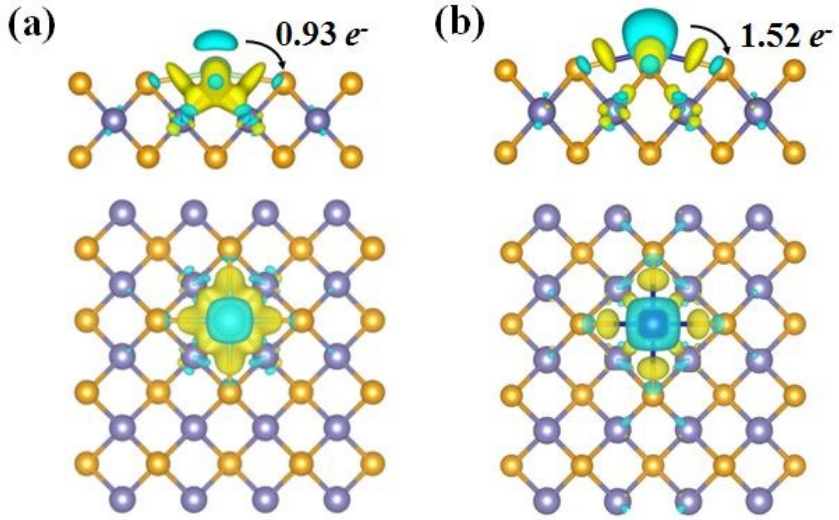

Fig. 4 Charge density difference for Li (a) and Mg (b) adsorbed FeSe monolayer at **A** site. The isosurface value is set to be 0.002 eÅ^{-3}.

As it is important for an electrode material to maintain the conductive character upon metal atom adsorption, we further examined the electronic properties of FeSe monolayers with different metal atoms adsorption at the energetically most favorable **A** site (Fig. S10). The adsorption of the metal atom only slightly influences the electronic band structure of the pristine FeSe monolayer: the metallic feature of the FeSe monolayer is preserved. The well maintained electronic conductivity is rather beneficial to the performance of metal ion batteries.

3.3 The diffusion of the single *M* (*M* = Li, Na, K, Mg, and Ca) atom on the FeSe monolayer

The charging/discharging rate correlates dominantly with the transport properties of the ions and electrons, depending on the Li, Na, K, Mg, and Ca diffusion and electrical conductivity of the FeSe nanosheet. Thus, it is necessary to estimate the diffusion of metal atoms on the surface of the FeSe monolayer. In this regard, we investigated the diffusion barriers of metal atoms on the FeSe monolayer. Since **A** site is energetically most favorable among the three adsorption sites (**A**, **B** and **C**), taking the symmetry of the FeSe monolayer into considered, we examined two diffusion pathways connecting two neighboring **A** sites (Fig. 5a): Path-I (**A**–**B**–**A**), where the metal atom moves across a **B** site; Path-II (**A**–**C**–**A**), where the metal atom migrates across a **C** site. Similar diffusion pathways were chosen in previous theoretical studies.[66]

According to our calculations, Path-II (**A**–**C**–**A** route) has very large diffusion barriers (0.47~2.48 eV) for all examined metal atoms, while the energy barriers along Path-I (**A**–**B**–**A** route**)** are significantly reduced. Remarkably, FeSe monolayer exhibits rather low diffusion barriers for Li, Na, and K atoms through Path-I pathway (0.16, 0.13, and 0.11 eV, respectively). Compared to the DFT reported single Li diffusion barrier of 0.22/0.25/0.36 eV on the $VS_2/MoS_2/Ti_3C_2F_2$ monolayer,[25,67,68] the FeSe monolayer can exhibit faster transport and higher charge/discharge rate for Li, and even for other alkali elements. The common commercial anode materials, graphite and TiO_2 polymorphs, need to overcome a diffusion barrier about 0.35~0.65 eV for Li.[69,70] Note that the monolayer FeSe has excellent ion mobility compared with bulk FeSe phase, in which the diffusion barriers of Li, Na, and K are 0.20, 0.46, and 0.82 eV, respectively.[49] Moreover, the diffusion barrier of the alkali metal atoms

View Article Online
DOI: 10.1039/D0CP00967A

decreases from 0.16 eV for Li to 0.11 eV for K, in the same trend as found on the Cr_2CO_2 monolayer,[71] but in a reversed trend when compared with FeSe bulk phase due to the repulsion against both upper and lower monolayers in the bulk.[49] Compared to the monovalent alkali metal atoms (Li, Na and K), the diffusion barrier for Mg and Ca are 0.85 and 1.53 eV, which are much higher than that for Li, Na and K, respectively. Thus, the FeSe monolayer facilitates a faster transport for alkali metal atoms, indicating an enhanced rate capability for alkali metal-based batteries.

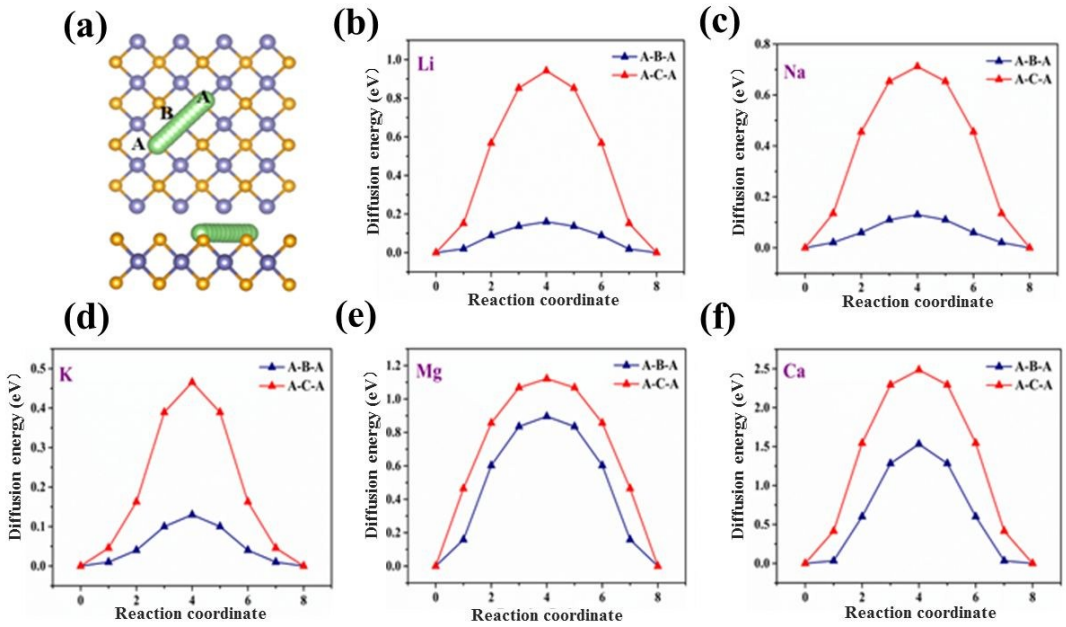

Fig. 5 (a) The diffusion pathways for a metal atom on the FeSe monolayer (from A sites to another A sites). The diffusion barrier profiles of (b) Li, (c) Na, (d) K, (e) Mg and (f) Ca on the FeSe monolayers.

3.4 Theoretical storage capacity and open-circuit voltage

The average open circuit voltage (OCV) and the storage capacity (*C*) are two important characteristics for rechargeable metal ion batteries, which can be calculated

View Article Online
DOI: 10.1039/D0CP00967A

based on the charge-discharge mechanism. The charge-discharge mechanism of FeSe-based metal ion battery can be described as the following half-cell reaction:

$$\mathrm{FeSe} + xM^{n+} + xne^{-} \leftrightarrow M_x\mathrm{FeSe} \qquad (3)$$

The Gibbs free energy change of this half-cell reaction was used to determine the average open circuit voltage (OCV). Herein, the Gibbs free energy was approximately simplified into the internal energy (ΔE), because $P\Delta V$ is only on the order of 10^{-5} eV and the entropy term ($T\Delta S$) is around 25 meV at room temperature.[72] The average OCV can be derived from the average adsorption energy (E_{ave}) as,[68]

$$\mathrm{OCV} = -E_{\mathrm{ave}}/xne \qquad (4a)$$

$$E_{\mathrm{ave}} = E_{M_x\mathrm{FeSe}} - E_{\mathrm{FeSe}} - xE_{M\text{-bulk}} \qquad (4b)$$

where E_{FeSe}, $E_{M_x\mathrm{FeSe}}$, and $E_{M\text{-bulk}}$ are the energy of monolayer FeSe, the total energy of M-adsorbed FeSe, the energy per atom in the bulk metal M, respectively, and n is the valence states of fully ionized metal atoms from the electrolyte.[73] For example, n = 1 for Li, Na, and K; n = 2 for Mg, Ca. The symbol x is the chemical ratio of M atom, and the maximum value of x is determined by gradually increasing the metal atom on the FeSe monolayer as the previous work.[74] The corresponding adsorption capacities were calculated by the following equation:

$$C = xnF/\mathrm{M}_{M_x\mathrm{FeSe}} \qquad (5)$$

where F is the Faraday constant (26801 mA h mol^{-1}), and $\mathrm{M}_{M_x\mathrm{FeSe}}$ is the molar weight of M_xFeSe. Therefore, it is important to reveal the structure of M_xFeSe with respect to various x values, thus, to determine the proper values of $E_{M_x\mathrm{FeSe}}$ and $\mathrm{M}_{M_x\mathrm{FeSe}}$.

Note that multi-layer metal adsorption on the anode is possible, as exemplified by the case of surface functionalized MXenes, on which multi-layer Li/Na/Mg/Al adsorption significantly enhances the metal storage capacity.[75] Thus, to estimate the largest metal storage capacity, we added more than one layer of metal atoms on the

View Article Online
DOI: 10.1039/D0CP00967A

FeSe monolayer. Based on the FeSe 2×2×1 supercell ($Fe_{16}Se_{16}$), the Li-ion battery was selected as an example to explain the process of gradually adding metal atoms on the FeSe surface. Attaching a Li atom at the site **A** on one surface of the $Fe_{16}Se_{16}$ results in a low-limit chemical formula Li_xFeSe (x = 0.0625, Fig. 6a). Our computations showed that Li atoms tend to bond to both surfaces of the FeSe monolayer when occupying the **A** sties (Fig. S11-S13). After all the **A** sites of two surfaces are occupied, Li atoms start to occupy the **B** sites at the second Li atom layer, and the **C** sites at the third Li atom layer. Thus, several possible configurations with both surfaces exposed to metal atoms were carefully considered for Li_xFeSe systems with higher x values (x = 0.25, 0.5, 1, 2, 3, and 4). The same approach was used to constructed FeSe systems with other intercalated metal atoms (M = Na, K, Mg, and Ca).

In order to illustrate the most stable adsorption configuration of metal atoms (M = Li, Na, K, Mg, and Ca) at different adsorption concentration on the FeSe monolayer, we calculated the formation energies (E_f) of M_xFeSe (M = Li, Na, K, Mg, and Ca) compounds with respect to FeSe monolayer and Li/Na/K/Mg/Ca bulk metals as the reference states based on the equation:[76]

$$E_f(x) = (E_{Mx\text{FeSe}} - E_{\text{FeSe}} - xE_{M\text{-bulk}})/(x+1),\ M = \text{Li, Na, K, Mg, and Ca} \qquad (6)$$

where $E_{Mx\text{FeSe}}$, E_{FeSe}, and $E_{M\text{-bulk}}$ are total energy of M-adsorbed FeSe, the energy of monolayer FeSe, and the energy per atom in the bulk metal M, respectively. We plotted the convex energy hull, the curve of formation energies of all the configurations considered *vs.* the concentrations of M (x) in the intercalated FeSe systems (Fig. S14). The most stable configurations for each concentration we considered, as presented in Figure 6, are located on the hull with negative formation energies, and thus thermodynamically stable, while those above the hull are

metastable. These data further confirm the stability of Li_4FeSe, Na_4FeSe, K_3FeSe, MgFeSe, and Ca_3FeSe.

We found that increasing the x value gradually reduces the E_{ave} value, indicating the decreased thermodynamic stability of M_xFeSe (Fig. S15), which is attributed to the electrostatic repulsion among the adsorbed metal atoms. When the Li/Na atoms are stacked up to three layers over both surfaces of FeSe (x = 4, Fig. 6g, Table S5), the E_{ave} values for Li and Na are still more negative than the corresponding cohesive energy of bulk metals, thus the maximum value of x for Li and Na is 4. Following the same procedure, we determined that K and Ca atoms can build up to two layers over both surfaces of FeSe, corresponding to x = 3 (Fig. 6f). In comparison, FeSe monolayer has rather poor adsorption capacity for Mg: only one layer **A** sites on both surfaces of FeSe can be adsorbed strongly (x = 1, Fig. 6d). Overall, the maximum ratio of M atoms adsorbed on both surfaces of FeSe can be concluded into the following chemical formulas: Li_4FeSe, Na_4FeSe, K_3FeSe, MgFeSe, and Ca_3FeSe.

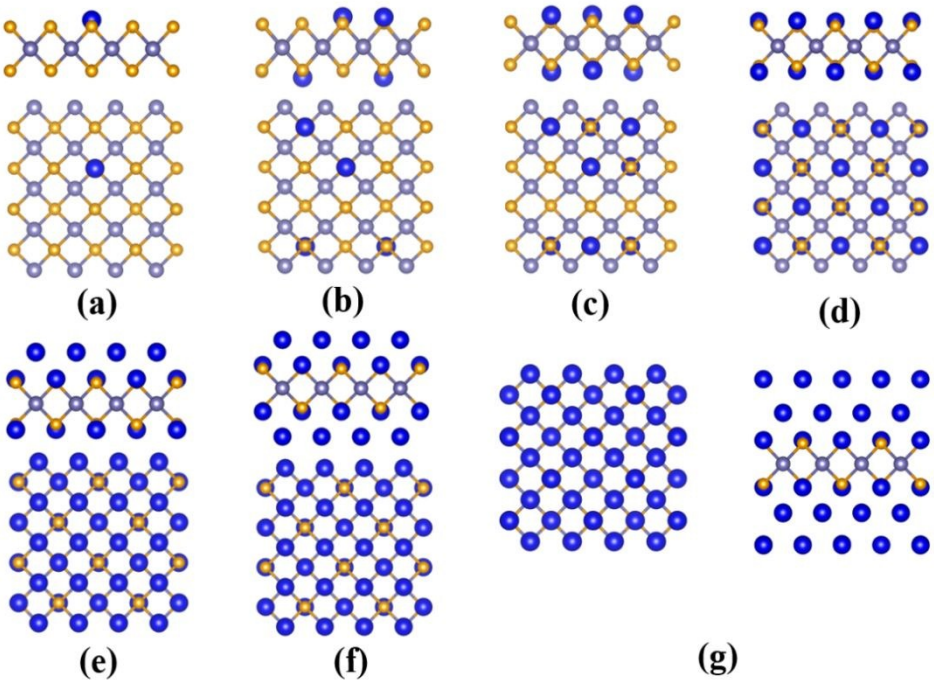

Fig. 6 Side and top views of the optimized atomic structures for (a) $Li_{0.0625}FeSe$, (b) $Li_{0.25}FeSe$, (c) $Li_{0.5}FeSe$, (d) LiFeSe, (e) Li_2FeSe, (f) Li_3FeSe, and (g) Li_4FeSe. Other M_xFeSe have similar structures.

Finally, we calculated the average open circuit voltage (OCV) and the storage capacity for *M*-ion batteries at various *x* values based on equations 4(a,b) and 5. Fig. 7 depicts the calculated OCVs as a function of the adatom concentration represented by *x* in the M_xFeSe. As the value of *x* increases, the storage capacities on anode for all *M*-ion batteries increases, while the average OCV on anode decreases. We unveiled that the maximum specific capacities of Li, Na, K, Mg, and Ca are calculated to be 658, 473, 315, 339, and 631 mAh g^{-1}, respectively. These results are found to be larger in comparison to other 2D anode materials, such as graphite (372 mA h g^{-1} for Li,[77] 284 mA h g^{-1} for Na,[78] 273 mAh g^{-1} for K [79]), α-FeSe (340 mA h g^{-1} for Li)[49], phosphorene (389.02 mA h g^{-1} for Li, 315.52 mA h g^{-1} for Na, 310.71 mA h g^{-1} for Mg),[21] MXenes (447.8 mA h g^{-1} for Li, 351.8 mA h g^{-1} for Na, 191.8 mA h g^{-1} for K, and 319.8 mA h g^{-1} for Ca)[20] or 2D-MoS_2 (146 mA h g^{-1} for Na).[80]

Considering that the OCV values by GGA+U are typically higher than those by GGA, and better agree with the experimental measurements,[81] we computed average OCVs of Li, Na, and K at the PBE+U level. The PBE+U computed OCV values (0.88, 0.49, and 0.38 V for Li, Na, and K, respectively; the corresponding values at PBE are 0.25, 0.17 and 0.14 eV) are relatively high and are in a good range. The higher potential is practically critical because it relieves the risk of the dendrite formation. For Li, the average OCV is between those of the commercial anode materials, 0.11 V for graphite [77] and 1.50~1.80 V for TiO_2.[70] The average voltage of Na is also in a desirable voltage range for a sodium anode of 0.00~1.00 V,[82] and the average voltage of K is also closer to the K insertion in graphite at about 0.17 V.[79] Note that the

View Article Online
DOI: 10.1039/D0CP00967A

calculated OCVs on FeSe monolayer for Li, Na, and K are lower than those in the bulk FeSe (1.0 V).[49] Thus, these OCV values suggest significant feasibility for FeSe monolayer to be applied as LIBs, NIBs, and KIBs anodes. As for Mg and Ca, the computed average OCV are low (0.04 V and 0.08 V), which suggest easy formation of the undesirable solid electrolyte interface (SEI). Thus, though FeSe shows a fairly good capacity for Mg and Ca, it might not be a suitable anode material for Mg and Ca-ion batteries. From the above discussions, when the average open circuit voltage and the specific capacity are included for consideration, the monolayer FeSe is suitable for anode materials of Li, Na, and K-ion batteries.

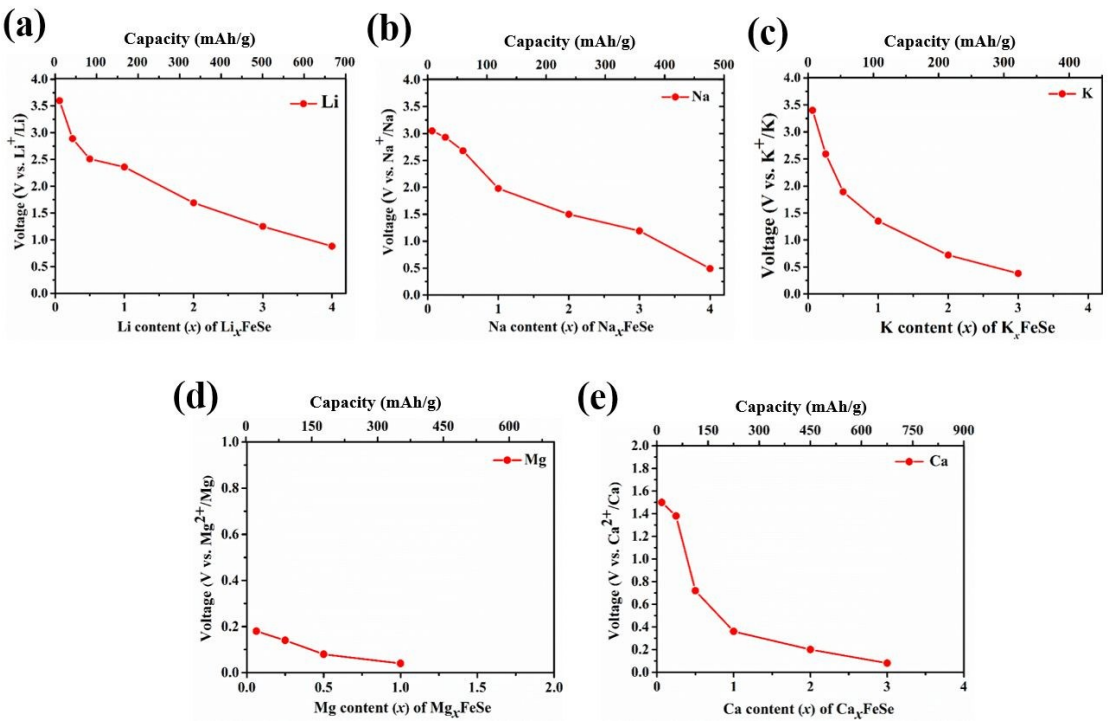

Fig. 7 The calculated voltage profiles of FeSe monolayers at different metal atoms adsorption degrees for (a) Li, (b) Na, (c) K, (d) Mg and (e) Ca at PBE+U level.

3.5 The safety of the FeSe monolayer as an anode material

View Article Online
DOI: 10.1039/D0CP00967A

The volume change (expansion and contraction) of anode materials is a big concern since it can cause fracture in anode materials, and eventually result in significant capacity fading during charging and discharging process. To estimate the effects of *M* (*M* = Li, Na, K, Mg, and Ca) adsorption on the volume change of the FeSe monolayer, we examined the in-plane expansion of the FeSe single-layer (Table S6, Fig. S16). Expectedly, the lattice parameter increases as the *M* adsorption increases. The in-plane lattice expansions for the maximum adsorption of Li, Na, K, Mg and Ca are 3.90 %, 5.50 %, 5.79 %, 4.25 %, and 5.99 %, respectively. Obviously, the bigger the atomic radius, the larger the lattice expansion for the atoms in the same periodic group. For example, with the largest radius among the alkali metals examined here, K adsorption leads to a pronounced in-plane lattice expansion of 5.79%. Note that the volume changes of the FeSe monolayer upon adsorption/desorption of Li and non-Li atoms are smaller than the corresponding value for graphite during the lithiation/delithiation process (typically in the order of 10 %),[83] indicating that the expansion/contraction in the FeSe monolayer during metal atom intercalation/deintercalation is a not a worrying issue.

The FeSe monolayer also exhibits good structure stability under *M* adsorption, since no structural distortion of the FeSe monolayer was found with the increase of *M* (Li, Na, K, Mg, and Ca) adsorption concentration (Fig. 6). Inspired by the high theoretical capacity and favorable OCVs of FeSe monolayer as the anodes for Li, Na, and K ion batteries, we further investigated the structural stability of fully intercalated FeSe electrode at room temperature by performing FPMD simulations in NVT at 300

View Article Online
DOI: 10.1039/D0CP00967A

K (the structures at the end of 5 ps simulations are given in Fig. S17). In all these intercalated systems, the FeSe monolayer structure is well retained after 5 ps FPMD simulations. Note that neither significant deformation nor bond breakage occurs in the FeSe monolayer during Li, Na and K intercalation, and the adsorbed metal atoms only slightly deviate from their equilibrium positions. When all the Li/Na/K atoms are removed from the intercalated FeSe structure, MD simulations of this slightly distorted FeSe monolayer can quickly recover its planar configuration, implying the good thermal stability of the FeSe monolayer during Li/Na/K ionintercalation/extraction.

Conclusions

By means of DFT computations, we explored the feasibility of using the intrinsically metallic FeSe monolayer as anode materials for metal (Li, Na, K, Mg, and Ca) ion batteries. The results revealed that the FeSe monolayer is most suitable as anode materials for Li, Na, and K-ion batteries, it can adsorb three layers of Li and Na, two layers of K, and the calculated maximum specific capacities reach up to 658, 473 and 315 mA h g^{-1}, and Li, Na, and K atoms show fast diffusions on the FeSe monolayer with the low energy barriers of 0.16, 0.13, and 0.11 eV, respectively, indicating the moderate charge/discharge rate. Moreover, the average OCVs of FeSe monolayer for LIBs, NIBs and KIBs are relatively low, which fall into a suitable range (0.38~0.88 V), the charge/discharging platform can be avoided. Considering the high theoretical charge capacity, low energy barriers, robust structural stability and moderate OCV for Li, Na, and K, we conclude that FeSe holds great potential as a high-performance anode materials for Li-, Na-, and K-ion batteries.

View Article Online
DOI: 10.1039/D0CP00967A

Conflicts of interest

There are no conflicts of interest to declare.

Acknowledgements

This work was supported in China by the National Nature Science Foundation of China (Nos. 11828401, 11464032, 11964022) and Startup Project of Inner Mongolia University, and in USA by NASA (Grant Number 80NSSC19M0236) and NSF Center for the Advancement of Wearable Technologies (Grant 1849243).

Supplementary Information

The PBE+U band structure and DOS of the FeSe sheet; The total energy of FeSe monolayer AFM states as a function of lattice constant; The top and side views of FeSe monolayer at the end of 5 ps FPMD simulation at 500 K, 700 K, 1000 K and 1500 K. Sides views of the optimized structures of FeSe monolayer after adsorbing different metal atoms at **B** and **C** sites; The charge density differences for the examined metal atoms adsorbed on FeSe monolayer at **B** and **C** sites; Computed band structures of adsorbed FeSe monolayer; Side and top views of different configurations for $Li_{0.125}FeSe$, $Li_{0.187}FeSe$, $Li_{0.25}FeSe$ as well as the relative energies; The convex energy hulls of M_xFeSe; The average adsorption energies of the adsorbed metal atoms as a function of the x values; The lattice constant variation as the function of M concentration x; The side views of the intercalated FeSe electrode by Li, Na , and K atoms at the end of FPMD simulation at 300 K; The calculated relative energies (in eV) of Li adsorbed on FeSe monolayer; In-plane stiffness, the Young's modulus of the FeSe monolayers; The electron transfer (in e^-) from the metal atoms (M = Li, Na, K, Mg and Ca) to the FeSe monolayer and the Cl atom in their chlorides; The average adsorption energy for M multi-layer adsorption in the stoichiometry of M_xFeSe and the cohesive energy of M in bulk phase; Lattice expansion during the intercalation process of LIBs, NIBs, KIBs, MIBs, and CIBs.

View Article Online
DOI: 10.1039/D0CP00967A

References

1 H. Wang, H. Feng and J. Li, *Small*, 2014, **10**, 2165–2181.

2 J. M. Tarascon and M. Armand, *Nature*, 2001, **414**, 359–367.

3 H. Li, Z. Wang, L. Chen and X. Huang, *Adv. Mater.*, 2009, **21**, 4593–4607.

4 M. Liang and L. Zhi, *J. Mater. Chem.*, 2009, **19**, 5871–5878.

5 J.-Y. Hwang, S.-T. Myung and Y.-K. Sun, *Chem. Soc. Rev*., 2017, **46**, 3529–3614.

6 J. M. Tarascon, *Nature Chem.*, 2010, **2**, 510.

7 G. Zhou, F. Li and H.-M. Cheng, *Energy Environ. Sci*., 2014, **7**, 1307–1338.

8 M. Á. Muñoz-Márquez, D. Saurel, J. L. Gómez-Cámer, M. Casas-Cabanas, E. Castillo-Martínez and T. Rojo, *Adv. Energy Mater*., 2017, **7**, 1700463.

9 K. Kubota and S. Komaba, *J. Electrochem. Soc.*, 2015, **162**, 2538–2550.

10 C. Vaalma, D. Buchholz and S. Passerini, *Current Opinion Electrochem*., 2018, **9**, 41–48.

11 M. S. Park, J. G. Kim, Y. J. Kim, N. S. Choi and J. S. Kim, *Israel J. Chem.*, 2015, **55**, 570–585.

12 A. Ponrouch and M.R. Palacin, *Current Opinion Electrochem*., 2018, **9**, 1–7.

13 W. Wang, W. Li, S. Wang, Z. Miao, H. K. Liu and S. Chou, *J. Mater. Chem. A*, 2018, **6**, 6183–6205.

14 L. Li, Y. Zheng, S. Zhang, J. Yang, Z. Shao and Z. Guo, *Energy Environ. Sci*., 2018, **11**, 2310–2340.

15 M. S. Whittingham, *Chem. Rev*., 2004, **104**, 4271–4301.

16 Y. Jing, Z. Zhou, C. R. Cabrera and Z. Chen, *J. Mater. Chem. A*, 2014, **2**, 12104–12122.

17 L. Peng, Y. Zhu, D. Chen, R. S. Ruoff and G. Yu, *Adv. Energy Mater*., 2016, **5**, 1600025.

18 S. Mukherjee and G. Singh, *ACS Appl. Energy Mater*., 2019, **2**, 932−955.

19 B. Anasoi, M. R. Lukatskaya and Y. Gogotsi, *Nat. Rev. Mater*., 2017, **2**, 16098.

20 D. Er, J. W. Li, M. Naguib, Y. Gogotsi and V. B. Shenoy, *ACS Appl. Mater. Interfaces*, 2014, **6**, 11173−11179.

21 A. Sibari, A. Marjaoui, M. Lakhal, Z. Kerrami, A. Kara, M. Benaissa, A. Ennaoui, M. Hamedoun, A. Benyoussef and O. Mounkachi, *Sol. Energ. Mat. Sol. C*., 2018, **180**, 253−257.

View Article Online
DOI: 10.1039/D0CP00967A

22 S. Stankovich, D. A. Dikin, G. H. B. Dommett, K. M. Kohlhaas, E. J. Zimney, E. A. Stach, R. D. Piner, S. B. T. Nguyen and R. S. Ruoff, *Nature*, 2006, **442**, 282−286.

23 C. Xu, B. Xu, Y. Gu, Z. Xiong, J. Sun and X. S. Zhao, *Energy Environ. Sci*., 2013, **6**, 1388−1414.

24 G. Kucinskis, G. Bajars and J. Kleperis, *J. Power Sources*, 2013, **240**, 66−79.

25 Y. Jing, Z. Zhou, C. R. Cabrera and Z. Chen, *J. Phys. Chem. C*, 2013, **117**, 25409–25413.

26 J. Mei, T. Liao and Z. Q. Sun, *J. Energ. Chem*., 2018, **27**, 117−127.

27 H. Hwang, H. Kim and J. Cho, *Nano Lett*., 2011, **11**, 4826−4830.

28 S. Ding, D. Zhang, J. S. Chen and X.W. D. Lou, *Nanoscale*, 2012, **4**, 95−98.

29 K. F. Mark, C. Lee, J. Hone, J. Shan and T. F. Heinz, *Phys. Rev. Lett*., 2010, **105**, 136805.

30 Y. Jing, E. O. Ortiz-Quiles, C. R. Cabrera, Z. Chen and Z. Zhou, *Electrochim. Acta*, 2014, **147**, 392−400.

31 J. Zhou, J. Lin, X. Huang, Y. Zhou, Y. Chen, J. Xia, H. Wang, Y. Xie, H. Yu, J. Lei, F. Liu, Q. Zeng, C.-H, Hsu, C. Yang, L. Liu, T. Yu, Z. Shen, H. Lin, B. I. Yakobson, K. Suenaga, G. Liu and Z. Liu, *Nature*, 2018, **556**, 355−362.

32 M. J. Winiarski, J. Zasada and M. Samsel-Czekala, *Comp. Mater. Sci*., 2018, **142**, 372−376.

33 F.-C. Hsu, J.-Y. Luo, K.-W. Yeh, T.-K. Chen, T.-W. Huang, P. M. Wu, Y.-C. Lee, Y.-L. Huang, Y.-Y. Chu, D.-C. Yan and M.-K. Wu, *Proc. Natl. Acad. Sci.*, 2008, **105**, 14262−14264.

34 D. Liu, W. Zhang, D. Mou, J. He, Y.-B. Ou, Q.-Y. Wang, Z. Li, L. Wang, L. Zhao, S. He, Y. Peng, X. Liu, C. Chen, L. Yu, G. Liu, X. Dong, J. Zhang, C. Chen, Z. Xu, J. Hu, X. Chen, X. Ma, Q. Xue and X. J. Zhou, *Nat. Commun*., 2012, **3**, 931.

35 B. Lei, J. H. Cui, Z. J. Xiang, C. Shang, N. Z. Wang, G. J. Ye, X.G. Luo, T. Wu, Z. Sun and X. H. Chen, *Phys. Rev. Lett*., 2016, **116**, 077002.

36 M. B. Lucas, D. G. Free, S. J. Sedlmaier, J. D. Wright, S. J. Cassidy, Y. Hara, A. J. Corkett, T. Lancaster, P. J. Baker, S. J. Blundell and S. J. Clarke, *Nat. Mater*., 2013, **12**, 15−19.

37 W. Si, Z.-W. Lin, Q. Jie, W.-G. Yin, J. Zhou, G. Gu, P. D. Johnson and Q. Li, *Appl. Phys. Lett*., 2009, **95**, 052504.

View Article Online
DOI: 10.1039/D0CP00967A

38 F. Nabeshima, Y. Imai, M. Hanawa, I. Tsukada and A. Maeda, *Appl. Phys. Lett.*, 2013, **103**, 172602.

39 J.-F. Ge, Z.-L. Liu, C. Liu, C.-L. Gao, D. Qian, Q. K. Xue, Y. Liu and J.-F. Jia, *Nat. Mater.*, 2015, **14**, 285−289.

40 K. Hanzawa, H. Sato, H. Hiramatsu, T. Kamiya and H. Hosono, *Proc. Natl. Acad. Sci.*, 2016, **113**, 3986−3990.

41 S. He, J. He, W. Zhao, L. Zhao, D. Liu, X. Liu, D. Mou, Y.-B. Ou, Q.-Y. Wang, Z. Liu, L. Wang, Y. Peng, Y. Liu, C. Chen, L. Yu, G. Liu, X. Dong, J. Zhang, C. Chen, Z. Xu, X. Chen, X. Ma, Q. K. Xue and X. J. Zhou, *Nat. Mater.*, 2013, **12**, 605−610.

42 Z. F. Wang, H. Zhang, D. Liu, C. Liu, C. Tang, C. Song, Y. Zhong, J. Peng, F. Li, C. Nie, L. Wang, X. J. Zhou, X. Ma, Q. K. Xue and F. Liu, *Nat. Mater.*, 2016, **15**, 968−973.

43 Z. F. Wang, Z. Liu, J. Yang and F. Liu, *Phys. Rev. Lett.*, 2018, **120**, 156406.

44 B. Lei, N. Z. Wang, C. Shang, F. B. Meng, L. K. Ma, X. G. Luo, T. Wu, Z. Sun, Y. Wang, Z. Jiang, B. H. Mao, Z. Liu, Y. J. Yu, Y. B. Zhang, and X. H. Chen, *Phys. Rev. B*, 2017, **95**, 020503.

45 D. H. Wei, J. W. Liang, Y. C. Zhu, L. Hu, K. L. Zhang, J. J. Zhang, Z. Q. Yuan and Y. T. Qian, *Electrochem. Commun.*, 2014, **38**, 124−127.

46 T. Kajita, T. Noji, Y. Imai, T. Kawamata, M. Kato and Y. Koike, *J. Electrochem. Soc.*, 2018, **165**, A3582−A3585.

47 H. Abe, T. Noji, M. Kato and Y. Koike, *Physica C*, 2010, **470**, S487−S488.

48 B. C. Kim, K. Takada, N. Ohta, Y. Seino, L. Zhang, H. Wada and T. Sasaki, *Solid States Ionics*, 2005, **176**, 2383−2387.

49 Z. Jiang, X. Gu, L. Wang and L. Huang, *Chem. Phys. Lett.*, 2016, **659**, 230−233.

50 G. Kresse and J. Hafner, *Phys. Rev. B*, 1994, **49**, 14251−14269.

51 G. Kresse and J. Hafner, *Phys. Rev. B*, 1993, **47**, 558−561.

52 K. Albe and J. Furthmüller, *Phys. Rev. B*, 1996, **54**, 11169−11186.

53 P. E. Blöchl, *Phys. Rev. B*, 1994, **50**, 17953−17979.

54 J. P. Perdew, K. Burke and M. Ernzerhof, *Phys. Rev. Lett.*, 1996, **77**, 3865−3868.

55 S. Grimme, *J. Comput. Chem.*, 2006, **27**, 1787−1799.

56 H. J. Monkhorst and J. D. Pack, *Phys. Rev. B*, 1976, **13**, 5188−5192.

57 K. Momma, F. Izumi, J. Appl. Crystallogr, 2011, **44**, 1271−1276.

View Article Online
DOI: 10.1039/D0CP00967A

58 R. F. Bader, [M], Wiley Online Library, 1990.

59 G. Henkelman, A. Arnaldsson and H. Jonsson, *Comput. Mater. Sci.*, 2006, **36**, 354−360.

60 G. Henkelman and H. Jónsson, *J. Chem. Phys.*, 2000, **113**, 9901−9904.

61 G. Henkelman and H. Jónsson, *J. Chem. Phys.*, 2000, **113**, 9978−9985.

62 A. Georges, L. de's Medici and J. Mravlje, *Annu. Rev. Condens. Matter Phys.*, 2013, **4**, 137–178.

63 Amalia I. Coldea, Matthew D. Eatson, *Annu. Rev. Condens. Matter Phys.*, 2018, **9**, 125–146.

64 G. J. Martyna, M. L. Klein and M. Tuckerman, *J. Chem. Phys*., 1992, **97**, 2635−2643.

65 D. Huand and J. E. Hoffman, *Annu. Rev. Condens. Matter Phys*., 2017, **8**, 11−36.

66 (a) J. Zhou, H. Zhuang and H. Wang, *Nanoscale*, 2017, **9**, 17303−17311; (b) B. Zhang, Y. Huang, W. Bao, B. Wang, Q. Meng, L. Fan and Q. Zhang, *Phys. Chem. Chem. Phys.*, 2018, **20**, 25437−25445.

67 Y. Li, D. Wu, Z. Zhou, C. R. Cabrera and Z. Chen, *J. Phys. Chem. Lett.*, 2012, **3**, 2221−2227.

68 Q. Tang, Z. Zhou and P. Shen, *J. Am. Chem. Soc.* 2012, **134**, 16909–16916.

69 K. Persson, V. A. Sethuraman, L. J. Hardwick, Y. Hinuma, Y. S. Meng, A. van Der Ven, G. Ceder, *J. Phys. Chem. Lett*., 2010, **1**, 1176−1180.

70 Z. Yang, D. Choi, S. Kerisit, K. M. Rosso, D. Wang, J. Zhang, G. Graff, J. Liu, *J. Power Sources*, 2009, **192**, 588−598.

71 F. Li, C. R. Cabrera, J. Wang and Z. Chen, *RSC Adv.*, 2016, **6**, 81591–81596.

72 M. K. Aydinol, A. F. Kohan, G. Ceder, K. Cho and J. Joannopoulos, *Phys. Rev. B*, 1997, **56**, 1354–1365.

73 M. K. Aydinol, A. F. Kohan and G. Ceder, *J. Power Sources*, 1997, **68**, 664–668.

74 H. R. Jiang, Z. Lu, M. C. Wu, F. Ciucci and T. S. Zhao, *Nano Energy*, 2016, **23**, 97–104.

75 (a) Y. Xie, M. Naguib, V. N. Mochalin, M. W. Barsoum, Y. Gogotsi, X. Yu, K.-W. Nam, X.-Q. Yang, A. I. Kolesnikov and P. R. C. Kent, *J. Am. Chem. Soc.*, 2014, **136**, 6385–6394. (b) Y. Xie, Y. Dall'Agnese, M. Naguib, Y. Gogotsi, M. W. Barsoum, H. L. Zhuang and P. R. C. Kent, *ACS Nano*, 2014, **8**, 9606–9615.

View Article Online
DOI: 10.1039/D0CP00967A

76 (a) T. Bo, P. F. Liu, J. Xu, J. R. Zhong, Y. B. Chen, O. Eriksson, F. W. Wang, and B. T. Wang, *Phys. Chem. Chem. Phys*., 2018, **20**, 22168–22178; (b) T. Bo, P. F. Liu, J. Xu, J. R. Zhong, F. W. Wang and B. T. Wang, *Phys. Chem. Chem. Phys*., 2019, **21**, 5178–5188.

77 J. M. Tarascon and M. Armand, *Nature*, 2001, **414**, 359–367.

78 Y. Wen, K. He, Y. J. Zhu, F. D. Han, Y. H. Xu, I. Matsuda, Y. Ishii, J. Cumings and C. S. Wang, *Nat. Commun*., 2014, **5**, 4033.

79 Z. L. Jian, W. Luo and X. L. Ji, *J. Am. Chem. Soc*., 2015, **137**, 11566–11569.

80 M. Mortazavi, C. Wang, J. Deng, V. B. Shenoy and N. V. Medhekar, *J. Power Sources*, 2014, **5**, 279–286.

81 Y. S. Meng and M. E. Arroyo-de Dompablo, *Energy Environ. Sci.*, 2009, **2**, 589–690.

82 E. Yang, H. Ji and Y. Jung, *J. Phys. Chem. C*, 2015, **119**, 26347−26380.

83 J. Vetter, P. Novák, M. R. Wagner, C. Veitb, K.-C. Möller, J. O. Besenhard, M. Winter, M. Wohlfahrt-Mehrens, C. Vogler and A. Hammmouche, *J. Power Sources*, 2005, **147**, 269–281.

TOC